

# The effects of core-reflected waves on finite fault inversions with teleseismic body wave data

Yunyi Qian,<sup>1,2</sup> Sida Ni,<sup>3</sup> Shengji Wei,<sup>2,4</sup> Rafael Almeida<sup>2</sup> and Han Zhang<sup>1,3</sup>

<sup>1</sup>School of Earth and Space Sciences, University of Science and Technology of China, Hefei 230026, China. E-mail: [sdni@whigg.ac.cn](mailto:sdni@whigg.ac.cn)

<sup>2</sup>Earth Observatory of Singapore, Nanyang Technological University, Singapore 639798, Singapore

<sup>3</sup>State Key Laboratory of Geodesy and Earth's Dynamics, Institute of Geodesy and Geophysics, Wuhan 430077, China

<sup>4</sup>Asian School of the Environment, Nanyang Technological University, Singapore 639798, Singapore

Accepted 2017 August 2. Received 2017 July 29; in original form 2017 May 8

## SUMMARY

Teleseismic body waves are essential for imaging rupture processes of large earthquakes. Earthquake source parameters are usually characterized by waveform analyses such as finite fault inversions using only turning (direct)  $P$  and  $SH$  waves without considering the reflected phases from the core–mantle boundary (CMB). However, core-reflected waves such as  $ScS$  usually have amplitudes comparable to direct  $S$  waves due to the total reflection from the CMB and might interfere with the  $S$  waves used for inversion, especially at large epicentral distances for long duration earthquakes. In order to understand how core-reflected waves affect teleseismic body wave inversion results, we develop a procedure named Multitel3 to compute Green's functions that contain turning waves (direct  $P$ ,  $pP$ ,  $sP$ , direct  $S$ ,  $sS$  and reverberations in the crust) and core-reflected waves ( $PcP$ ,  $pPcP$ ,  $sPcP$ ,  $ScS$ ,  $sScS$  and associated reflected phases from the CMB). This ray-based method can efficiently generate synthetic seismograms for turning and core-reflected waves independently, with the flexibility to take into account the 3-D Earth structure effect on the timing between these phases. The performance of this approach is assessed through a series of numerical inversion tests on synthetic waveforms of the 2008  $M_w$  7.9 Wenchuan earthquake and the 2015  $M_w$  7.8 Nepal earthquake. We also compare this improved method with the turning-wave only inversions and explore the stability of the new procedure when there are uncertainties in *a priori* information (such as fault geometry and epicentre location) or arrival time of core-reflected phases. Finally, a finite fault inversion of the 2005  $M_w$  8.7 Nias–Simeulue earthquake is carried out using the improved Green's functions. Using enhanced Green's functions yields better inversion results as expected. While the finite source inversion with conventional  $P$  and  $SH$  waves is able to recover large-scale characteristics of the earthquake source, by adding  $PcP$  and  $ScS$  phases, the inverted slip model and moment rate function better match previous results incorporating field observations, geodetic and seismic data.

**Key words:** Waveform inversion; Body waves; Computational seismology; Earthquake source observations.

## 1 INTRODUCTION

In the past decade, large earthquakes such as the 2008 Wenchuan earthquake ( $\sim$ 110 s rupture duration; e.g. Xu *et al.* 2009; Feng *et al.* 2010), the 2011 Tohoku-Oki earthquake ( $\sim$ 150 s rupture duration; e.g. Simons *et al.* 2011; Wei *et al.* 2012) and the 2015 Illapel earthquake ( $\sim$ 100 s rupture duration; e.g. Li *et al.* 2016; Heidarzadeh *et al.* 2016) have caused catastrophic damages and heavy casualties. In these cases, reliable estimations of rupture processes provide valuable information for post-seismic rescue, tsunami alert, and studies of seismotectonics as well as earthquake

physics. The finite-source inversion has been widely used as an effective technique to reconstruct the spatial-temporal distribution of rupture processes (Hartzell & Heaton 1983; Ammon *et al.* 2011), and can be obtained by individual or joint inversion of seismic, geodetic and tsunami data sets (e.g. Ji *et al.* 2004; Shen *et al.* 2009). Among the above studies, teleseismic body waves ( $30^\circ$ – $90^\circ$ ), usually  $P$  and  $SH$  waves, have been used extensively in such inversions because their propagation is well understood and they are readily available for large earthquakes with a good range of coverage for both slowness and azimuth. Modelling of teleseismic direct  $P$  and  $SH$  waves, along with the associated free surface reflections ( $pP$ ,

$sP$ ,  $sS$ ), can be carried out efficiently using ray theory (Langston & Helmberger 1975). There are several numerical methods based on ray theory which allow for modelling of teleseismic body waves such as SYN (McCaffrey *et al.* 1991), TBW (Kikuchi & Kanamori 1991) or TEL3 (Chu *et al.* 2009). Recent developments in forward modelling techniques and algorithms in combination with enhanced coverage of global seismic networks make it possible to rapidly map the spatial and temporal slip distributions after a large earthquake.

Teleseismic body waves are essential observations for estimating the seismic source information after large earthquakes, but slip models derived from inversions with these measurements are not necessarily unique. For the 2008  $M_w 7.9$  Wenchuan earthquake, Hayes (2008, unpublished) generated a finite fault model (<http://earthquake.usgs.gov/earthquakes/eventpage/usp000g650#finite-fault>), based on teleseismic broad-band  $P$ ,  $SH$  phases and long period surface waves. He suggested that the rupture propagated unilaterally towards the northeast on the Pengguan Fault for about 100 km and on the segments of Beichuan Fault for about 270 km with a source duration of about 120 s. Zhang *et al.* (2008) used  $P$  wave data to show that this event had a bilateral rupture process with a duration of 93 s and was divided into five stages. Nakamura *et al.* (2010) indicated that the source fault was composed of at least two main fault segments with a 128 s source duration. Yagi *et al.* (2012) estimated a source duration of 125 s and proposed a slip history including six distinct subevents. Fielding *et al.* (2013) used  $P$ ,  $SH$  waveforms and geodetic data sets to generate a kinematic source model in which the rupture produced a cascade of subevents with a total duration of about 116 s. These inversion results mostly show that the peak energy release was around 25 s (some of these moment rate function results are shown in Fig. 1), with the main rupture occurring on a thrust fault (the Beichuan fault). Nevertheless, the total source durations (varying from 93 to 128 s; Fig. 1) and the shapes of slip distributions differ appreciably. The discrepancies could be attributed to a few factors: different types of data, station distribution, Green's function, model parameterization and inversion algorithms. The accuracy of the Green's functions is of particular importance. Wald & Graves (2001) found that inaccurate Green's functions biased inversion results even when abundant *a priori* information was provided. We will focus here on the impact of inaccurate Green's on finite fault inversions based on teleseismic body wave data.

For teleseismic body wave inversions in previous studies, Green's functions are usually generated based on ray theory using a given 1-D velocity model. These synthetics include turning waves such as  $P$  and  $SH$  phases, but not secondary phases such as core-reflected waves (e.g.  $PcP$  or  $ScS$ ), which can be identifiable in  $P$  and  $SH$  records. Yu *et al.* (2012) have observed clear  $ScS$  phases with energy comparable to direct  $SH$  phases for the 2008 Wenchuan earthquake. These core-reflected phases could potentially complicate the shape of recorded waveforms, especially at large distances where the time interval between direct and core-reflected phases is smaller than the time window used in inversions. One of the reasons why core-phases are not taken in account in conventional teleseismic inversions is that a large number of stations with good azimuth and distance distributions may suppress the influence of these secondary phases on source parameter determinations, as their slownesses are different from those of direct  $P$  or  $SH$  phases. Another issue is the complexity of core-reflected waves in observations, as their arrival times and shapes could be modified by complex structure of the core-mantle boundary (CMB) and the D'' layer (Borgeaud *et al.* 2016). Recently, Vallee *et al.* (2011) proposed a body-wave deconvolution approach to determine point source parameters, in which they added

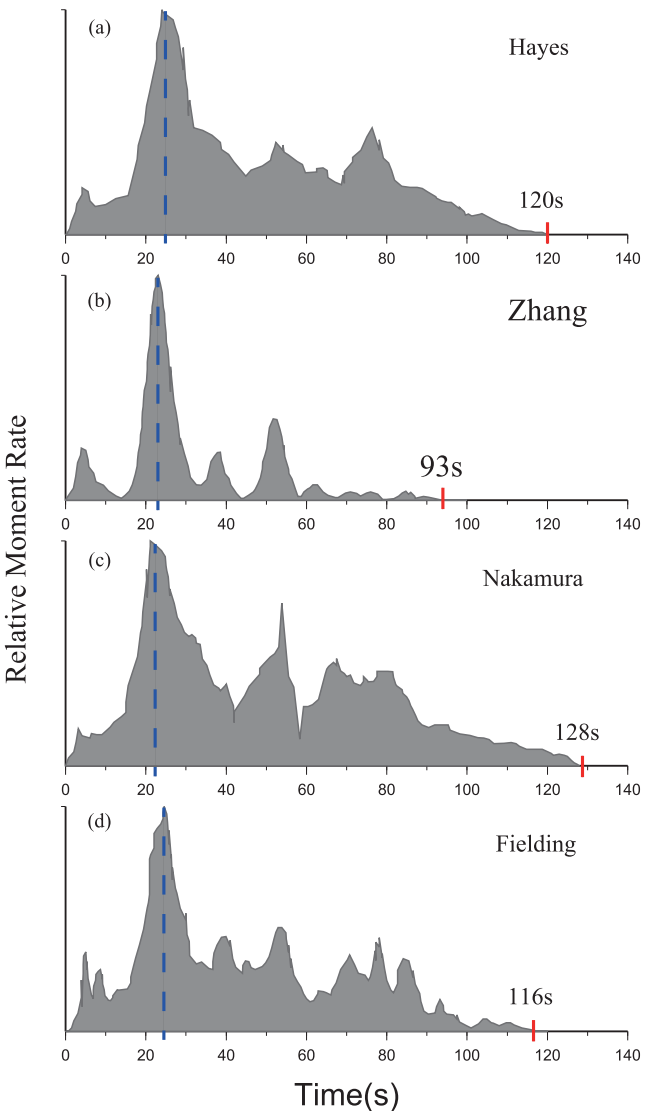


**Figure 1.** Various source duration estimates for the 2008 Wenchuan earthquake. Moment rate functions (a) from teleseismic broad-band  $P$  and  $SH$  phases and long period surface waves by Hayes (2008, unpublished), (b) from teleseismic  $P$  waves by Zhang *et al.* (2008), (c) from teleseismic  $P$  waves by Nakamura *et al.* (2010), (d) from teleseismic  $P$  and  $SH$  waveforms and geodetic data sets by Fielding *et al.* (2013). The blue dashed lines indicate the time of peak energy release, which is consistent among the different inversions. The red solid lines mark the end of the energy release, and the numbers above show the source durations.

core-reflected phases ( $PcP$ ,  $ScS$ ) and surface reflected  $PP$  phase in the Green's functions to estimate seismic moment magnitude, focal mechanism and source time functions for large earthquakes. This leads us to consider whether these phases could be used in finite fault inversions to study the rupture process for large earthquakes. It is difficult to model  $PP$  waveforms for distances shorter than  $60^\circ$  based on a 1-D velocity model, since there are triplication phases caused by mantle transition zone. For distances larger than  $60^\circ$ ,  $PP$  phases can be neglected since they arrive at least 130 s after the  $P$  wave and are usually outside of the inversion windows for most earthquakes.

In this study, we focus only on the effects of the core-reflected waves for large earthquakes with source durations around 100 s. If a ray-based approach could be adopted to generate Green's functions,

the arrival time and the amplitude calibrations for separated phases can be carried out independently, which allows  $PcP$  and  $ScS$  waves to be used in waveform modelling. We investigate whether the core-reflected waves affect finite fault inversions and whether the use of more accurate 1-D Green's functions could provide a better recovery of target models. In order to do this, we develop a new procedure for generating teleseismic Green's functions which contain both turning body waves (direct  $P$  and  $SH$  waves; depth phases  $pP$ ,  $sP$ ,  $sS$ ; along with crustal multi-reflected waves) and core-reflected phases ( $PcP$ ,  $ScS$ ;  $pPcP$ ,  $sPcP$ ,  $sScS$ ; and the associated reflections from the CMB). We also generate classic Green's functions with only turning  $P$  and  $SH$  waves for comparison. We plug these two types of Green's functions into a wavelet-domain finite fault inversion package (Ji *et al.* 2002) to compare the results. When other conditions are all the same, the differences between these results should reflect the influence of core-reflected phases in the Green's functions.

To quantify this effect, we first use synthetic waveforms generated from two target models as input data, one is a simplified model derived from the 2008 Wenchuan earthquake and the other one is a smooth model inverted from the 2015 Nepal earthquake. We then explore the influence of uncertainties in finite fault inversions, and discuss the adaptability of our newly developed method for travel-time calibration using aftershocks when complex structures exist in the interior of the Earth. Finally, we test our approach with observations of the 2005  $M_w 8.7$  Nias–Simeulue earthquake, which has a well characterized rupture model derived from a joint inversion of field observations, geodetic and seismic data (Briggs *et al.* 2006; Hsu *et al.* 2006; Konca *et al.* 2008).

## 2 METHODOLOGY

Since Olson & Apsel (1982) introduced the finite-fault inversion approach to obtain the source model of the 1979 Imperial Valley earthquake, many inversion techniques have been developed to study the spatial and temporal slip distribution of large earthquakes. The inversion process has been done either in the time domain (e.g. Kikuchi & Kanamori 1986; Chen & Xu 2000; Hartzell *et al.* 2013) or the frequency domain (e.g. Olson & Anderson 1988; Cotton & Campillo 1995; Pratt 1999). More recently, Ji *et al.* (2002) presented a new procedure to transform both data and synthetic seismograms into the wavelet domain and then conduct waveform modelling with the separated segments in different frequencies. This method allows to extract more information about slip heterogeneity, and can simultaneously and efficiently invert for slip amplitude, slip direction, rise time, and rupture velocity. Many earthquakes have been studied with this inversion method, for example, the 2002 Denali earthquake (e.g. Tsuboi *et al.* 2003), the 2011 Tohoku earthquake (e.g. Wei *et al.* 2012) and the 2013 Lushan earthquake (e.g. Hao *et al.* 2013; Liu *et al.* 2013). We use the wavelet domain inversion algorithm of Ji *et al.* (2002) to test the impacts of core-reflected waves on finite fault inversions.

At teleseismic distances, the modelling of direct  $P$  and  $SH$  Green's functions along with depth phases ( $pP$ ,  $sP$ ,  $sS$ ) can be carried out efficiently using standard ray methods. Here we use a hybrid technique based on ray theory and a propagator matrix Fig. 2(a), called Multitel3, to calculate body waves that include both turning waves (direct  $P$ ,  $pP$ ,  $sP$ , direct  $S$  and  $sS$ ) and core-reflected waves ( $PcP$ ,  $pPcP$ ,  $sPcP$ ,  $ScS$  and  $sScS$ ) phases. These synthetics also contain crustal reverberations. We generate two sets of Green's functions: one is the classic Green's function with only turning  $P$  and  $SH$  waves, while the other includes core-reflected waves. We

then plug both sets of Green's function into Ji's finite fault inversion package.

For a source depth  $h$  and an epicentre distance  $\Delta$ , the Green's function  $Green(h, \Delta, \omega)$  in the frequency domain with any angular frequency  $\omega$  at a receiver is the product of three terms: the impulse crustal response of source  $R_s(h, \Delta, \omega)$  and receiver  $R_r(h, \Delta, \omega)$ , and the impulse mantle response  $R_m(h, \Delta, \omega)$  along the ray path

$$Green(h, \Delta, \omega) = R_s(h, \Delta, \omega)R_m(h, \Delta, \omega)R_r(h, \Delta, \omega) \quad (1)$$

In eq. (1), the two terms for the source and receiver crustal regions can be represented with the Haskell propagator matrix described in by Haskell (1960, 1962) and Bouchon (1976). The mantle propagation, expressed in eq. (2), takes into account geometrical spreading  $G(h, \Delta)$  and anelastic attenuation  $Q(h, \Delta, \omega)$ , with an additional term of reflection coefficient  $Ref(h, \Delta)$  for core-reflected waves. Specifically, the reflection coefficient for  $ScS$  phase in transverse component is always 1 due to complete reflection from CMB:

$$R_m(h, \Delta, \omega) = G(h, \Delta)Q(h, \Delta, \omega)[Ref(h, \Delta)] \quad (2)$$

The geometrical spreading factor is deduced from a reference 1-D Earth model, incident angle, take-off angle, epicentre distance and their derivatives. We use  $t^*$  factors to represent attenuations of  $P$  and  $SH$  waves in mantle, which is defined as an integration of the travel time of the ray  $T_i$  and  $Q$  value  $Q_i$  in every layer:

$$Q(h, \Delta, \omega) = e^{-\frac{\omega}{2}t^*(h, \Delta, t)} = e^{-\frac{\omega}{2} \sum_{i=1}^N \frac{T_i(h, \Delta)}{Q_i}}. \quad (3)$$

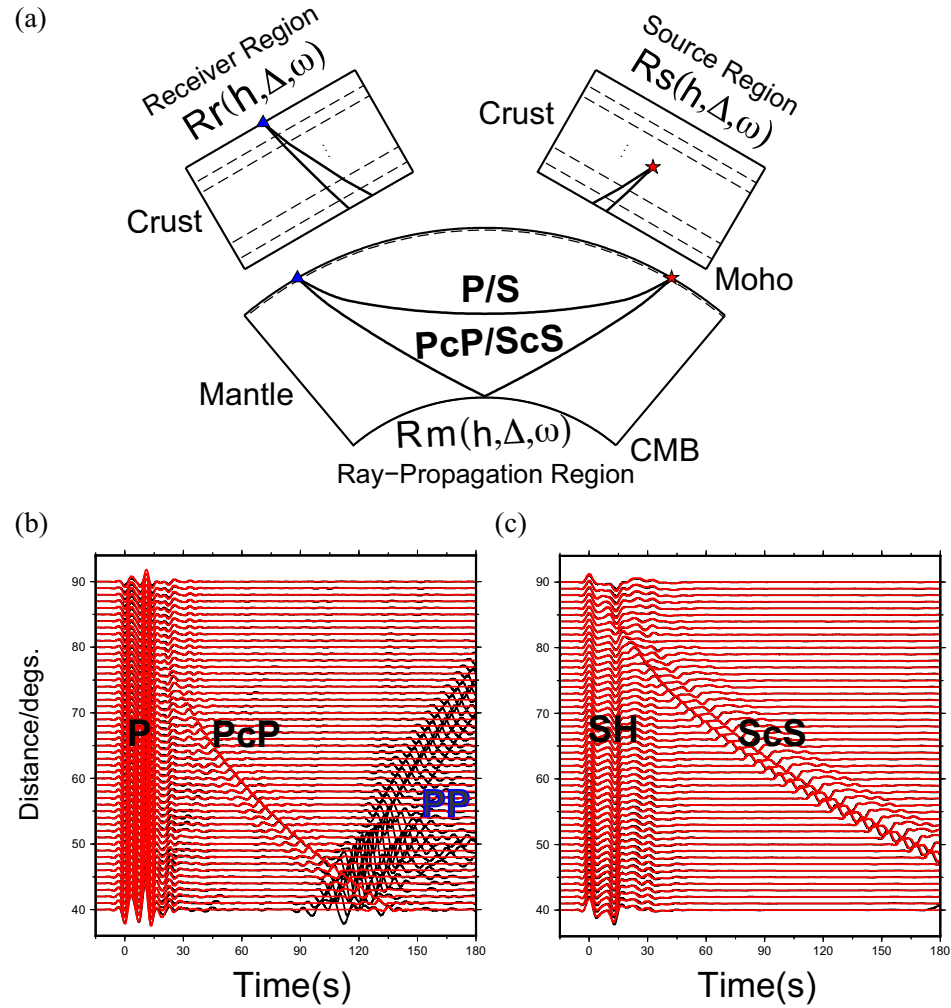
The above parameters are computed for each specific phase ( $P$ ,  $SH$ ,  $PcP$ , or  $ScS$ ), and the differential time between direct phase and corresponding core-reflected phases are calculated with 1-D ray-tracing or can be shifted from an external calibration table.

To benchmark our results, we compare the ray-based Green's function with full waveform synthetics obtained from a frequency-wavenumber integration method, called FK (Zhu & Rivera 2002). With a 1-D Earth model, it takes Multitel3 less than 1 min to generate teleseismic turning and core-reflected waves, while FK spent 5 hr to generate the synthetic full waveforms Fig. 2(b). Comparisons of vertical  $P$  and tangential  $SH$  waveforms for a vertical dip-slip fundamental source show that the arrival times and amplitudes of turning and core-reflected phases fit well with each other in the frequency range of 0.01–0.2 Hz (Figs 2b and c).

## 3 WAVEFORM MODELLING AND NUMERICAL INVERSION TESTS

### 3.1 Effects of core-reflected phases on observations

Yu *et al.* (2012) have demonstrated that  $ScS$  amplitudes are comparable with that of direct  $S$  waves at some azimuthal ranges for megathrust earthquakes, such as the  $SH$  waveforms recorded in the German Regional Seismic Network (GRSN) for the 2008  $M_w 7.9$  Wenchuan earthquake Fig. 3(a). To reduce artefacts caused by these secondary phases, they proposed an iterative algorithm to isolate  $S$  and  $ScS$  phases before using the records in inversions. Here, we solve the problem of contamination of secondary phase by adding core-reflected phases in the Green's functions. Using a finite fault source model of 2008 Wenchuan earthquake Fig. 3(b) from the United States Geological Survey (USGS), we generate two sets of synthetic  $SH$  waveforms with and without  $ScS$  phases. The crustal model is extracted from Crust2.0 (Bassin *et al.* 2000), and mantle model from PREM (Dziewonski & Anderson 1981).



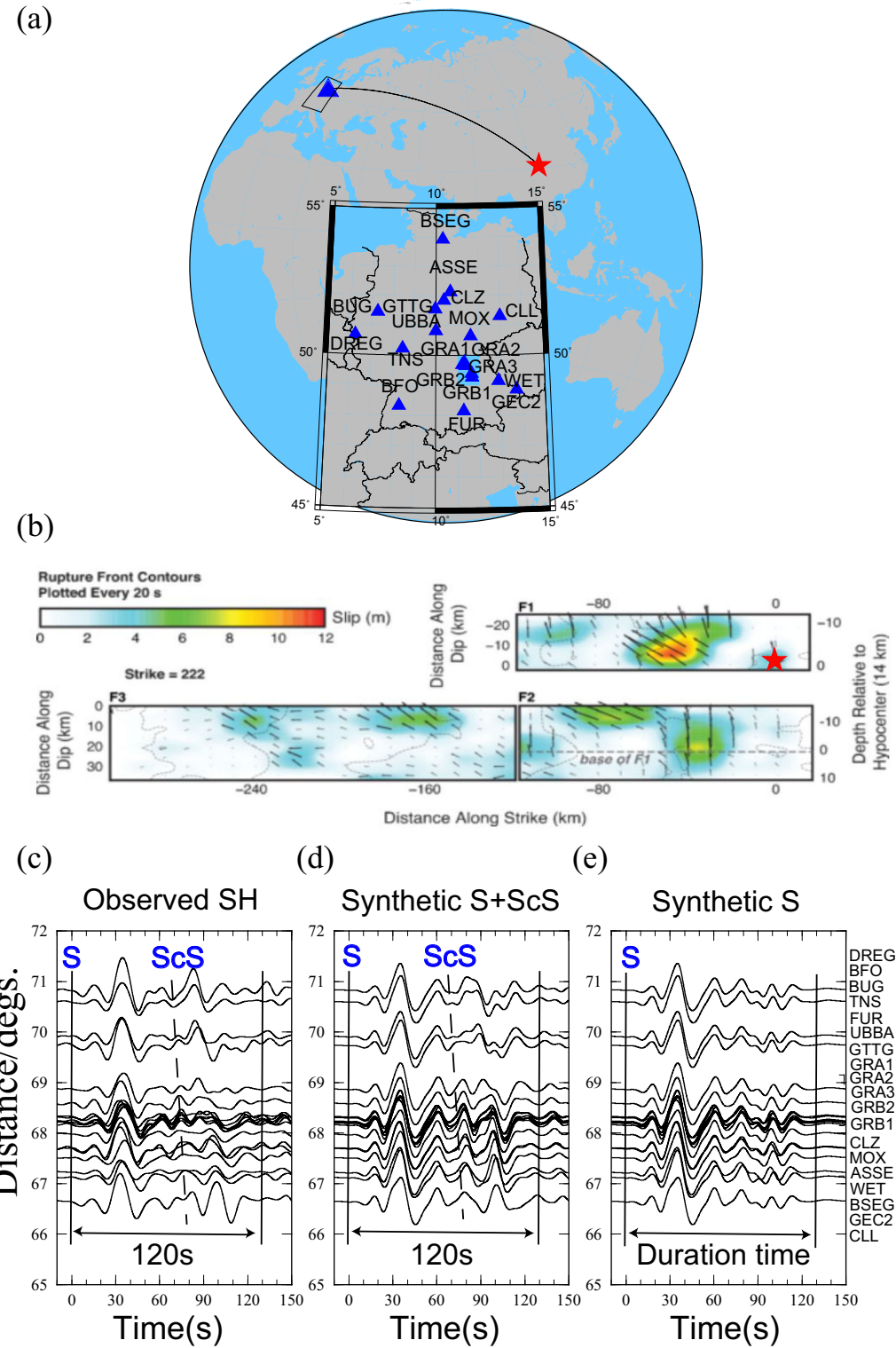
**Figure 2.** Schematic drawing to show teleseismic body waves containing turning and core-reflected phases. (a) Wave propagation factors in source region, receiver region and mantle paths. (b,c) Comparison of the Green's functions (red) of  $P$  and  $SH$  waves with waveforms generated by FK (black). Waveforms filtered with band of 0.01–0.2 Hz.

Fig. 3 shows the waveforms aligned on the direct  $S$  phases (first solid lines), including the observed waveforms Fig. 3(c), the synthetic waveforms with turning and the core-reflected phases Fig. 3(d) and synthetic waveforms with only turning waves Fig. 3(e). The observed  $SH$  waveforms show a clear arrival (dashed line in Fig. 3c) that probably corresponds to  $ScS$  waves. These arrivals might introduce artefacts in the finite fault inversion if  $ScS$  is not included in the Green's functions. By comparing the observations to the synthetic data, with Fig. 3(d) and without Fig. 3(e) the  $ScS$  phase, we confirm that the slowness of this arrival matches  $ScS$  wave. This demonstrates that these core-reflected phases from the early rupture overlap with the turning  $S$  waves from the later rupture at differential times around 70–80 s and epicentre distance between  $71^\circ$  and  $66^\circ$ .

### 3.2 Effects of core-reflected phases on finite fault slip models

In this section we conduct numerical inversion tests to quantify the effects of core-reflected phases on finite fault inversion results. We use a simplified rupture model Fig. 4(a) for the 2008  $M_w 7.9$  Wenchuan earthquake (with an initial thrust rupture, oblique-slip

afterwards and strike-slip finally) to generate synthetic data with Multitel3, to be used as input data so as to test recoverability of the inversion. The fault plane is 300 km long with a strike of  $229^\circ$  and 45 km wide with a dip of  $30^\circ$ , and is divided into 180 subfaults ( $20 \times 9$ ) of  $15 \text{ km} \times 5 \text{ km}$ . We assign slip to occur on three rectangular asperities (A, B and C) in our target model. The rupture begins at the right edge of A and propagates to the left through B and C, with a constant rupture velocity of  $2.0 \text{ km s}^{-1}$  and a constant rise time of 6 s. Asperity A is near the epicentre and has a uniform slip of 8 m and a rake of  $90^\circ$ . Asperity B is in the middle, with 4 m of slip and a rake of  $135^\circ$ . Asperity C has a slip of 6 m and a rake of  $180^\circ$ . Using a source model based on Crust2.0 (Table 1) and the PREM (Dziewonski & Anderson 1981), we generate synthetic  $SH$  and  $P$  waves for teleseismic stations of the Global Seismographic Network (GSN) with a distance range of  $40^\circ$ – $90^\circ$  Fig. 4(b), including  $S+ScS$ , turning  $S$ , and  $ScS$  (Figs 4c–e) and  $P+PcP$ , turning  $P$ , and  $PcP$  (Figs 4f–h). Though it takes about 150 s for the rupture to propagate from asperity A to C, we can still observe some signals until 180 s (Figs 4d and g), due to crustal reverberations. When the epicentral distance is larger than  $50^\circ$  for  $SH$  waves and  $40^\circ$  for  $P$  waves, the differential times between the core-reflected phases and the direct body waves are shorter than the duration of earthquake, leading to an overlap of the core-reflected signal



**Figure 3.** SH Waveform comparisons for the 2008 Wenchuan earthquake. (a) The 2008 Wenchuan earthquake (red star) and seismic stations in GRSN (blue triangles). (b) The finite fault model provided by the USGS (<http://earthquake.usgs.gov/earthquakes/eventpage/usp000g650#finite-fault>). (c–e) Observed and synthetic SH waveforms, aligned on direct S phases (solid lines); the arrival times of ScS phases are marked with dashed lines.

from the early rupture and the direct wave signal from the later rupture.

We then conduct finite fault inversions with different sets of Green's functions. During inversions, we use the same constant rupture velocity and rise time as those in the input model, allow

slip values to vary from 0 to 9 m at an interval of 0.2 m, and constrain rake angles to vary among three fixed values (90°, 135° and 180°). The Green's functions used in Figs 5(a), (c) and (e) do not include core-reflected phases. The Green's functions used in the inversions shown in Figs 5(b), (d) and (f) are the same as those used

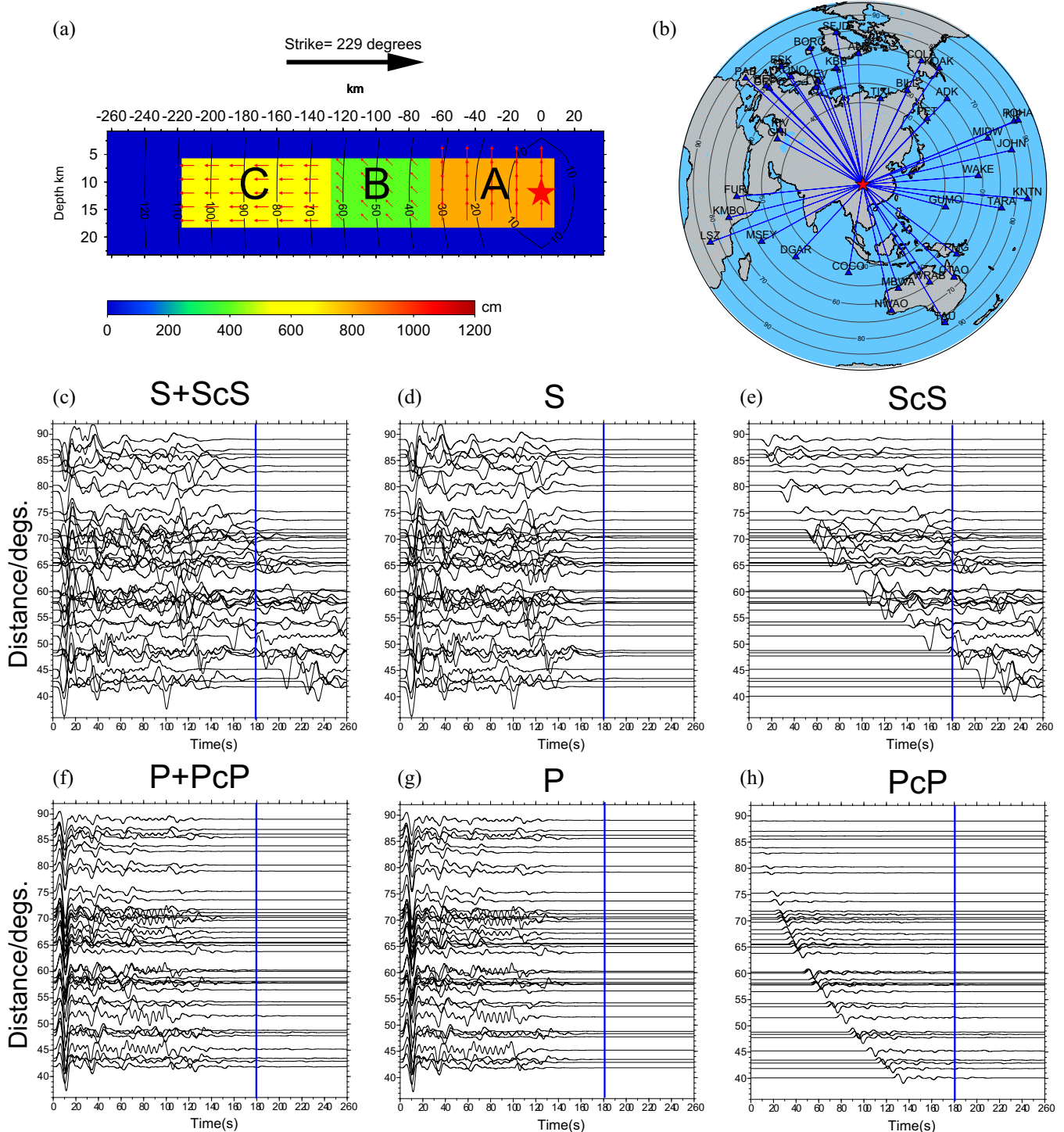


**Figure 4.** Synthetic teleseismic waves based on a simplified Wenchuan earthquake source model and real station distribution. (a) Slip distributions and isochron of the rupture front for the input source model with three asperities (A, B and C). Red star shows the epicentre location and red arrows indicate input slip vectors. (b) Hypocentre of the 2008 Wenchuan earthquake (red star) and modelled GSN stations (blue triangles). (c–h) Synthetic  $SH$  and  $P$  waveforms calculated by Multitel3: (c) and (f) are the input waveforms which contain both turning waves and core-reflected waves; (d) and (g) are turning  $SH$  and  $P$  waveforms, respectively; (e) and (h) are core-reflected waveforms,  $ScS$  and  $PcP$ , respectively. All traces are aligned on direct body waves ( $SH$  and  $P$  phases). Waveforms in (c) and (f) are input data for finite fault models.

to generate the synthetic input data (with core-phases). The comparison between the models in the two columns of Fig. 5 represents the impact of core-phases for  $ScS$  (a versus b),  $PcP$  (c versus d) and  $ScS+PcP$  (e versus f). The rupture arrest times derived from inversions with and without core-phases are similar with each other

( $\sim 110$  s), but the inverted slip distributions differ more from the target model when  $ScS$  or/and  $PcP$  phases are not included in the Green's functions. In other words, the inclusion of  $ScS$  and  $PcP$  in finite fault inversions improves the resolution of slip distributions. The contribution of  $PcP$  to the  $P$  inversion seems to be more

**Table 1.** The crustal model in the source region of the 2008  $M_w 7.9$  Wenchuan earthquake.

Vp (km s <sup>-1</sup> )	Vs (km s <sup>-1</sup> )	Rho (g cm <sup>-3</sup> )	Thickness (km)
2.50	1.10	1.20	1
4.00	2.10	2.40	1
6.10	3.50	2.75	20
6.30	3.60	2.80	20
7.20	4.00	3.10	4

significant than those of  $ScS$  to the  $S$  inversion. This phenomenon can be explained by the relationship between the focal mechanisms of the three subevents (asperities of A, B and C in Fig. 4a) and the radiation patterns of  $P$  waves (waveform amplitudes in Fig. 4g). The thrust slip of asperity A generates turning  $P$  waves with larger amplitudes, while the oblique-slip of asperity B and the strike-slip of asperity C subevents generate relatively small amplitude  $P$ -waves. These weaker  $P$  phases are easier to be contaminated by the  $PcP$  phases generated by the first asperity. The energy of turning phases in  $SH$  waveforms are usually strong, thus the  $SH$  inversion result is less influenced by  $ScS$  phases in this case. In Fig. 5(f), the inversion with  $SH+ScS$  and  $P+PcP$  provides the best recovery of the input slip model, as expected. Yet, the input model is not fully recovered, showing the limited resolving power of teleseismic body waves.

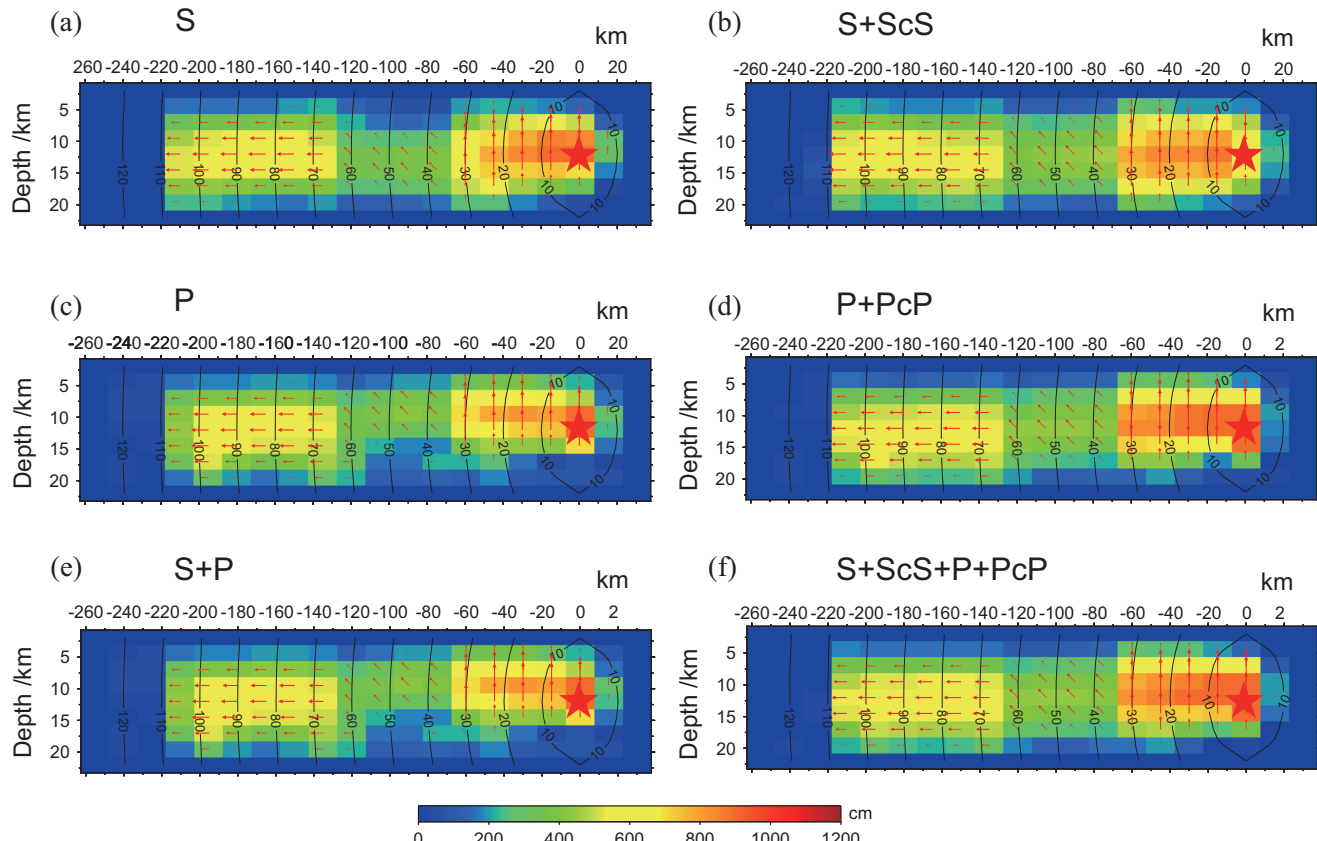


**Figure 5.** Finite fault models for simplified Wenchuan earthquake source with different Green's functions. (a)  $SH$  waveform inversion with only turning  $SH$  Green's functions. (b)  $SH$  waveform inversion with both turning  $SH$  and  $ScS$  Green's functions. (c)  $P$  waveform inversion with only turning  $P$  Green's functions. (d)  $P$  waveform inversion with both turning  $P$  and  $PcP$  Green's functions. (e) Joint inversion with turning  $SH$  and  $P$  Green's functions. (f) Inversion of  $SH$  and  $P$  waves and with  $S$ ,  $ScS$ ,  $P$  and  $PcP$  phases. The hypocentre is marked with a red star and the rupture time is indicated by black contours at intervals of 10 s. Red arrows indicate inverted slip vectors.

To assess performance of the slip inversions in these tests, we use a differential coefficient to quantify differences between the input model Fig. 4(a) and the inverted slip distributions along strike and dip (or depth) directions. We define the slip vector in each subfault with  $\vec{a}^{ij}$  as

$$\vec{a}^{ij} = [A_{ij} \cos \lambda_{ij}, A_{ij} \sin \lambda_{ij}]. \quad (4)$$

Where  $i$  is the  $i$ th subfault along strike, and  $j$  is the  $j$ th subfault along depth,  $A_{ij}$  and  $\lambda_{ij}$  represent slip amplitude and slip direction of the subfault  $ij$ . The differential coefficients along strike  $b_i$  and along depth  $b_j$  are expressed in eqs (5) and (6).

$$b_i = \frac{1}{N} \sum_{j=1}^n |\vec{a}_{\text{inverted}}^{ij} - \vec{a}_{\text{input}}^{ij}| \quad (5)$$

$$b_j = \frac{1}{M} \sum_{i=1}^m |\vec{a}_{\text{inverted}}^{ij} - \vec{a}_{\text{input}}^{ij}|. \quad (6)$$

Among all testing cases,  $N$  and  $M$  are two maximal values for the sum of differences between input and inverted slip vectors in each subfault along strike and depth, respectively; while  $n$  and  $m$  are the numbers of subfault along the two directions. A value of 0 indicates of a perfect match between the input and output model and a value of 1 represents the maximum observed difference between the target and inverted slip vector. The differential coefficients for the inversion results are displayed in Figs 6(a) and (b). The dashed

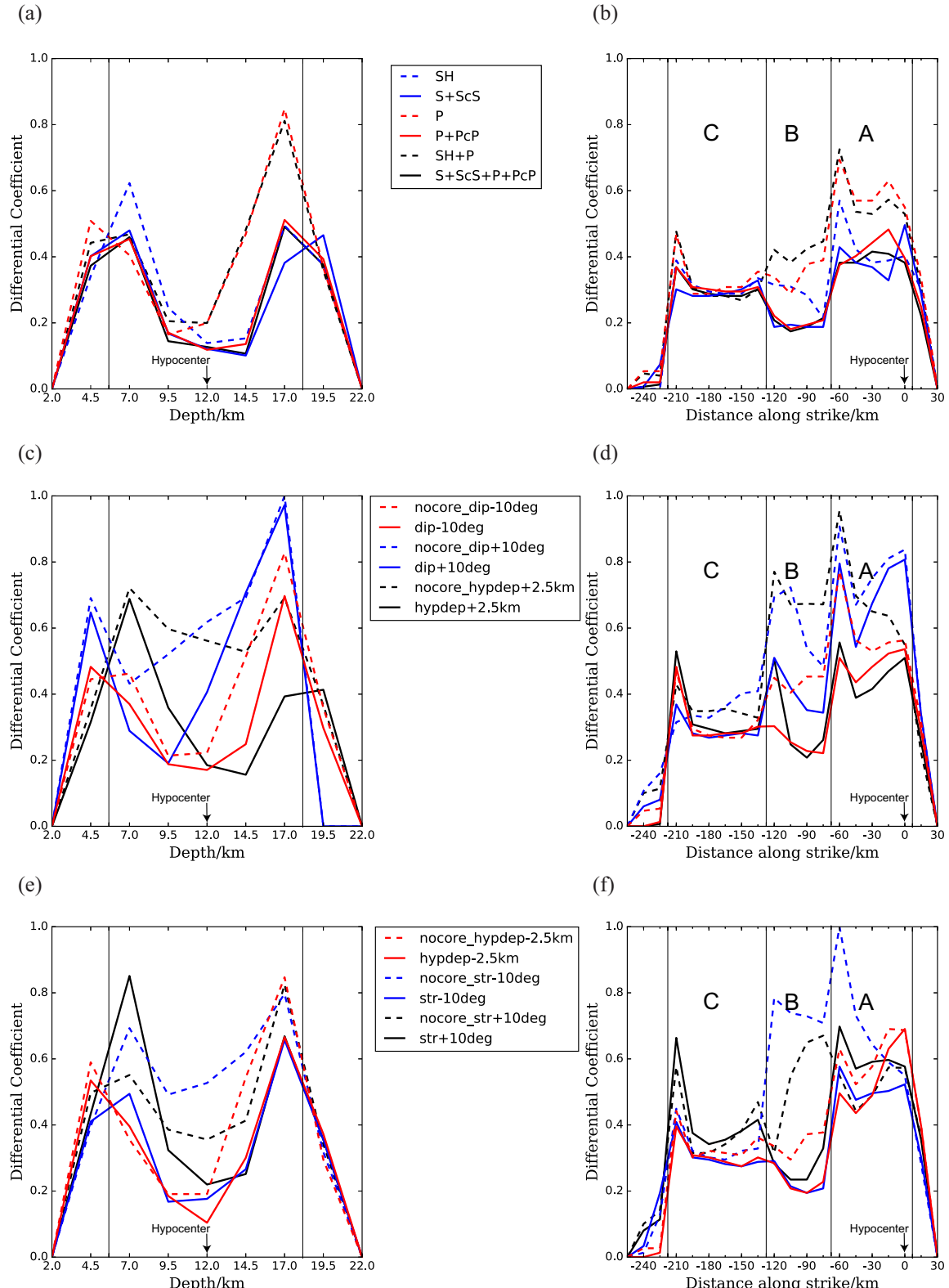


**Figure 6.** Comparison of inversion results along depth and strike directions. Differential coefficients along (a) depth direction (eq. 5) and (b) strike direction (eq. 6). (c-f) show effect of uncertainties in *a priori* information for the  $P+SH$  inversion results, (c) and (d) correspond to testing errors in dip angle of fault plane ( $\pm 10^\circ$ ) and hypocentre depth (+2.5 km), while (e) and (f) correspond to testing errors in hypocentre depth (-2.5 km) and strike angle of fault plane ( $\pm 10^\circ$ ). The dashed lines indicate the results are inverted without inclusion of core-reflected phases in the Green's functions, and the solid lines are the results when including them. Vertical black lines show the boundaries of asperities (A, B and C) along the two directions.

lines are the inversion results without core-reflected phases in the Green's functions (Figs 5a,c and e) and the solid lines are the results containing core-reflected phases in the Green's functions (Figs 5b, d and f). There are two peaks in the dip direction Fig. 6(a) and four peaks along strike Fig. 6(b) for all results. These coincide with the asperity boundaries (indicated by vertical black lines in Fig. 6) of the target model Fig. 4(a). The differential coefficients are consistently lower when we consider  $ScS$  and/or  $PcP$  phases in the Green's functions, with the largest improvement occurring for  $P$  wave inversion results at a depth of 17 km Fig. 6(a). The large variations from solid lines (with core-phases) to dashed lines (without core-phases) are seen for  $P$  wave inversions (red) and  $SH+P$  inversions (black), which locate around deeper part ( $\sim 12$  to  $\sim 19$  km in Fig. 6a) of the first two asperities (asperities A and B in Fig. 6b).

Based on the simplified input model Fig. 4(a), which has a sharp variations for slip vector (amplitude and rake angle) among the three asperities, a small degree of freedom on rake angle is adopted during these inversions in order to have stable results. However, in the case of real earthquakes, both slip and rake variations along rupture could be larger, and a large freedom on rake angle is required during inversions. Thus in the following synthetic tests, which have smooth input models and real earthquake inversions, we will adopt small intervals and greater range of possible values for both of slip amplitude and rake angle, respectively.

### 3.3 Effects of core-reflected phases on source duration and waveform error

The inversion tests above demonstrate the importance of core-reflected phases (especially  $PcP$ ) in rupture inversion for large earthquakes that have thrust-slip followed by strike-slip. We also conduct another synthetic case to study the influences of  $ScS$  individually due to its relative strong energy. For this, we use an inverted finite fault model of the 2015  $M_w 7.8$  Nepal earthquake Fig. 7(a) as our target source model. The source duration of this event is not too long, and it is straightforward to identify  $S$  and  $ScS$  phases making it possible to test their impacts individually. With this rupture model and a local source structure model extracted from Crust2.0 (Basson *et al.* 2000), we generate synthetic  $SH$  waves for GSN stations with a distance range of  $50^\circ$ – $90^\circ$  (Fig. 8). Our fault plane dimension is  $168\text{ km} \times 120\text{ km}$  with a strike of  $293^\circ$  and a dip of  $7^\circ$ , discretized into 315 subfaults ( $21 \times 15$ ) of  $8\text{ km} \times 8\text{ km}$ . During the inversions, we adopt the same fault geometry as the target model but use a fault plane with an along strike length twice that of the input one, so as to relax the prior constraint of fault length. We aim to determine whether there would be slip appearing in the latter part of the rupture due to  $ScS$ . We allow the rise time to change from 0.6 to 10.6 s with an interval of 1 s and the rupture velocity to vary from 2 to  $3\text{ km s}^{-1}$  at an interval of  $0.1\text{ km s}^{-1}$ . Slip value varies from 0 to 5 m at an interval of 0.2 m and rake angle changes from  $80^\circ$  to  $130^\circ$  at an interval of  $2.5^\circ$ . All of these parameters are in the same ranges as those in the input model.

Figs 7(b) and (c) show two finite fault inversions with different Green's functions (containing  $ScS$  phases, red traces in Fig. 8b; or not, red traces in Fig. 8a). The inversion using the Green's functions without  $ScS$  phases, has some artefacts, for example, a small slip patch around the 100 s rupture time contour in Fig. 7(b). This artefact, however, is not seen in Fig. 7(c), where  $ScS$  is included in the Green's functions. The difference can also be observed in the

moment rate function results Fig. 9(a) as a weak signal around 130–160 s (red line). Nevertheless, the  $ScS$  phases in the input data are not completely modelled as  $SH$  phases coming from later portion of artificial rupture Fig. 8(a), due to their different slowness. In summary, when we include  $ScS$  phases in the Green's functions, the slip distribution Fig. 7(c) and moment rate function (blue line in Fig. 9a) are closer to the input model (Fig. 7a and black line in Fig. 9a), and waveform misfit decreases from 7 per cent to 2 per cent.

## 4 SOURCES OF UNCERTAINTY

### 4.1 Impact of variations in fault geometry and hypocentre depth

The inclusion of the core-reflected phases during a finite fault inversion produce a better result, when accurate *a priori* information is known. The effect of uncertainty of various *a priori* conditions including source representation method and inversion set-up has been discussed in details in Shao & Ji (2012). Here, we will discuss other effects, such as the fault geometry and hypocentre depth adopted in inversion. In seismological studies, long period waveform analyses are usually first conducted to get a point source solution, which is then used to prescribe geometry of the rupture fault. Several agencies routinely provide focal mechanisms after the earthquakes, such as USGS and Global Centroid Moment Tensor (GCMT) catalogues. Empirical statistical results suggest that for a typical shallow earthquake, uncertainties of strike and dip angle among different results is around  $10^\circ$  (Helffrich 1997).

Here, we test the effect of uncertainties in earthquake source *a priori* parameters on the performance of including core-reflected phases (or not) in finite rupture inversions. For the 2008 Wenchuan earthquake, Figs 6(c)–(f) show how the differential coefficients increase when there are deviations in dip ( $\pm 10^\circ$ ), strike ( $\pm 10^\circ$ ) and hypocentre depth ( $\pm 2.5$  km), compared with values in Figs 6(a) and (b). This indicates that inaccurate *a priori* information can produce extra error in slip inversions. Nevertheless, most of the inversions with core-reflected phases (solid lines in Figs 6c–f) still yield better results, and have lower differential coefficients, than those without them (dashed lines in Figs 6c–f). To minimize these uncertainties, inclusion of existing geological field studies are important to further constrain fault geometries and obtain better inversion results. When available, regional geodetic data also can be combined with teleseismic waveforms to constrain fault geometry and hypocentre depth.

### 4.2 Influence of differential time between direct and core-reflected phase

Another issue is the uncertainty of differential time between direct and core-reflected phase, which depend on the Earth's interior structure. Teleseismic inversions with multiple phases rely on the assumption that the differential time between direct and subsequent phases is well predicted by a given Earth model. Nevertheless, the travel time of direct body waves and corresponding reflected phases from the CMB can be substantially different from predictions based on 1-D Earth models due to 3-D heterogeneity (Ritsema *et al.* 1998; Ni & Helmberger 2003). For example, the residual splitting in  $ScS$ , attributed to the D'' layer, shows lag times between 1.0 and 3.9 s (Wookey *et al.* 2005). For some ray paths sampling lateral heterogeneity of the upper mantle, the difference for  $ScS$  phase between

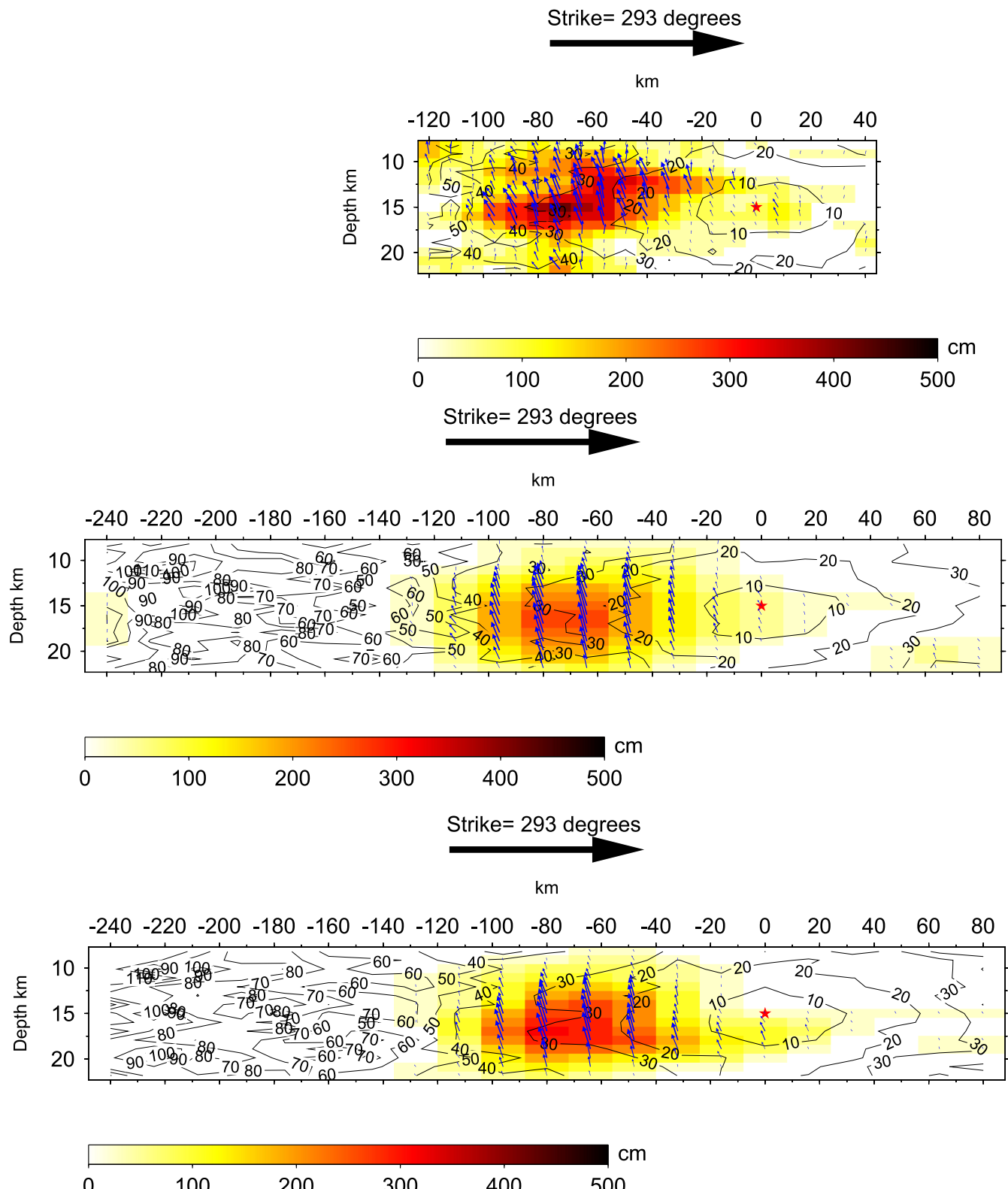


**Figure 7.** Comparison of input and inverted slip models for the 2015 Nepal earthquake. (a) The input rupture model of the 2015 Nepal earthquake from our inversion result with teleseismic body waves. (b) The inverted source model using Green's functions with  $SH$  turning wave only. (c) The inverted source model using Green's functions with both  $SH$  turning wave and core-reflected waves. The hypocentre is marked with a red star and the rupture time is indicated by black contours at intervals of 10 s. Blue arrows indicate inverted slip vectors.

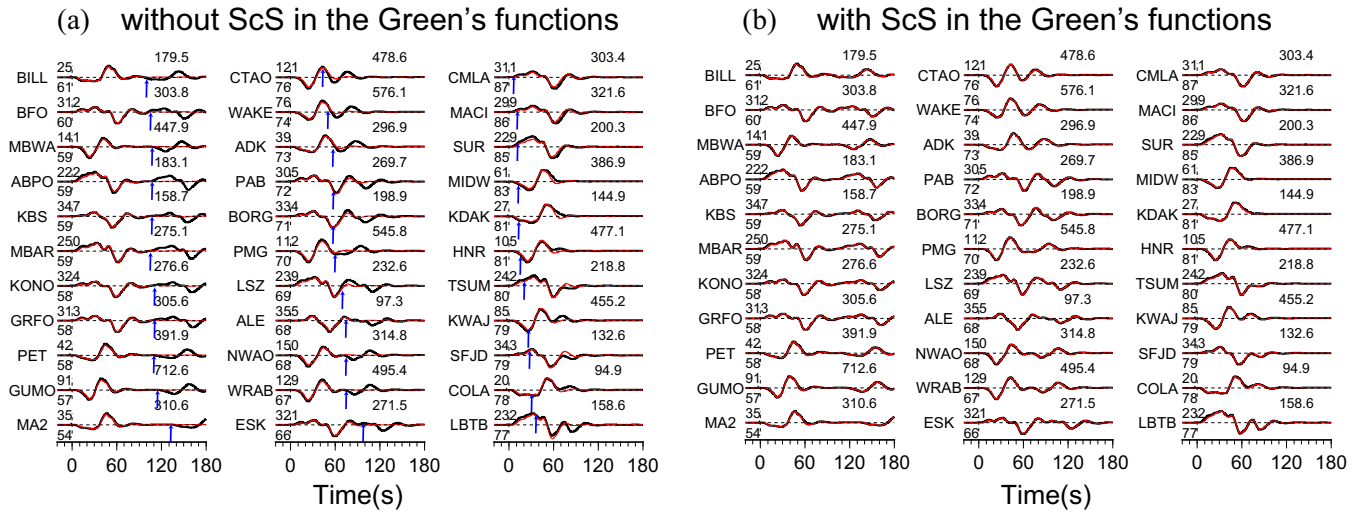


**Figure 8.**  $SH$  displacement waveforms for the 2015 Nepal earthquake. The source model of Fig. 7(a) is used to generate input data (black). (a) Waveforms inverted with turning  $SH$  Green's functions (red traces). Note the large difference between the input and modelled waveforms around the arrival times of  $ScS$  phases (shown by blue arrows). (b) Waveforms inverted with turning and core-reflected  $SH$  Green's functions (red traces) show a much better match to the input data. The station names are to the left of each trace. Numbers at the left of each seismogram are epicentral distance (under) and azimuth (upper) in degrees and numbers at the right of waveforms are maximum amplitude in micrometer.

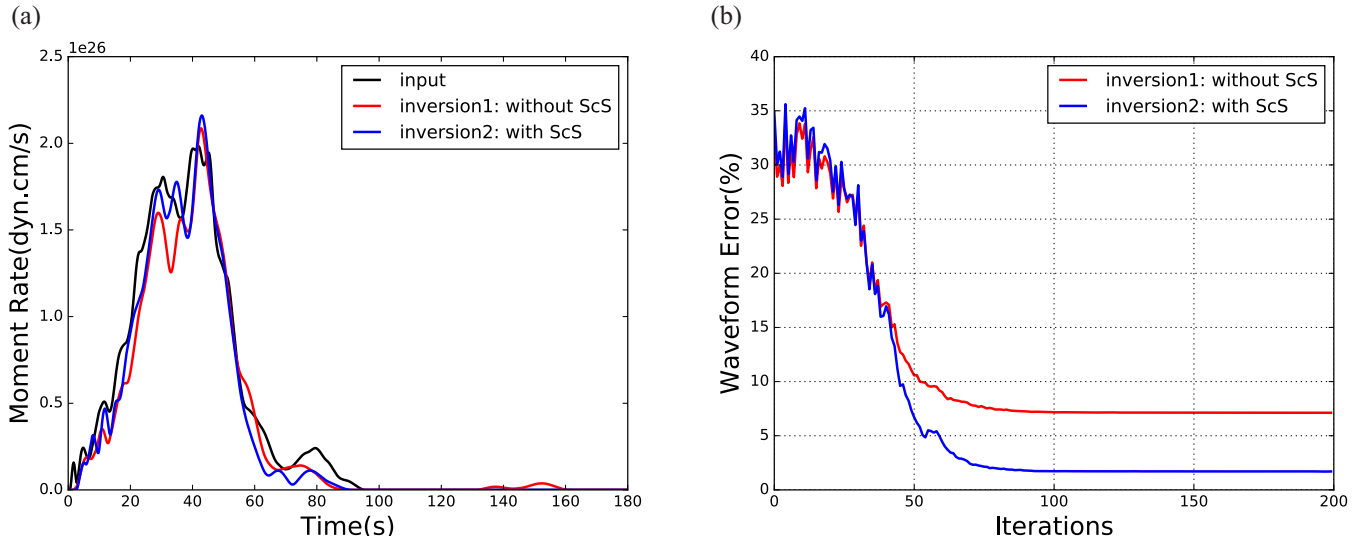


**Figure 9.** Comparison of moment rate function for different models of the 2015 Nepal earthquake, and inverted waveform misfits. (a) Input moment rate function (black), inverted results with turning  $SH$  waves (red) and with both of  $S$  and  $ScS$  waves (blue) in the Green's functions. (b) Waveform misfits for these two inversion tests along iterations of simulated annealing inversion.

oceanic and continental regions is estimated to be 4.5 s at maximum (Sipkin & Jordan 1976). These variations are a reason why core-phases are not taken into consideration in teleseismic body wave inversions.

To investigate how these uncertainties affects the inversions when core-reflected phases are not included in the Green's functions, we randomly change the arrival time of  $ScS$  phases in the input data of the 2015 Nepal case study with time variations between 2 s and 5 s, and then invert these synthetic data (Fig. 10). Some artefacts and greater waveform misfits are observed when  $ScS$  arrival time is not accurate, with the greatest misfit observed for 5 s error (Figs 10a–c). This indicates that inaccurate differential times between these phases can also result in artificial slip distribution and source duration. To address this problem, our approach has some intrinsic advantages as we compute turning (direct) and core-

reflected phases separately, thus we can apply an independently determined correction to the timing of core-phases easily. Such correction can be obtained from aftershocks and then applied to the main shock for the travel time variability due to 3-D Earth structure.

## 5 APPLICATION TO THE 2005 NIAS-SIMEULUE EARTHQUAKE

In order to test our approach, we proceed to study the 2005  $M_w$  8.7 Nias-Simeulue earthquake, which occurred in the Sunda subduction zone and lasted for more than 120 s according to USGS finite fault result. Therefore, the turning waves from the later rupture could overlap with the core-reflected phases from earlier rupture for some stations at large distance. Inversions from Global Positioning

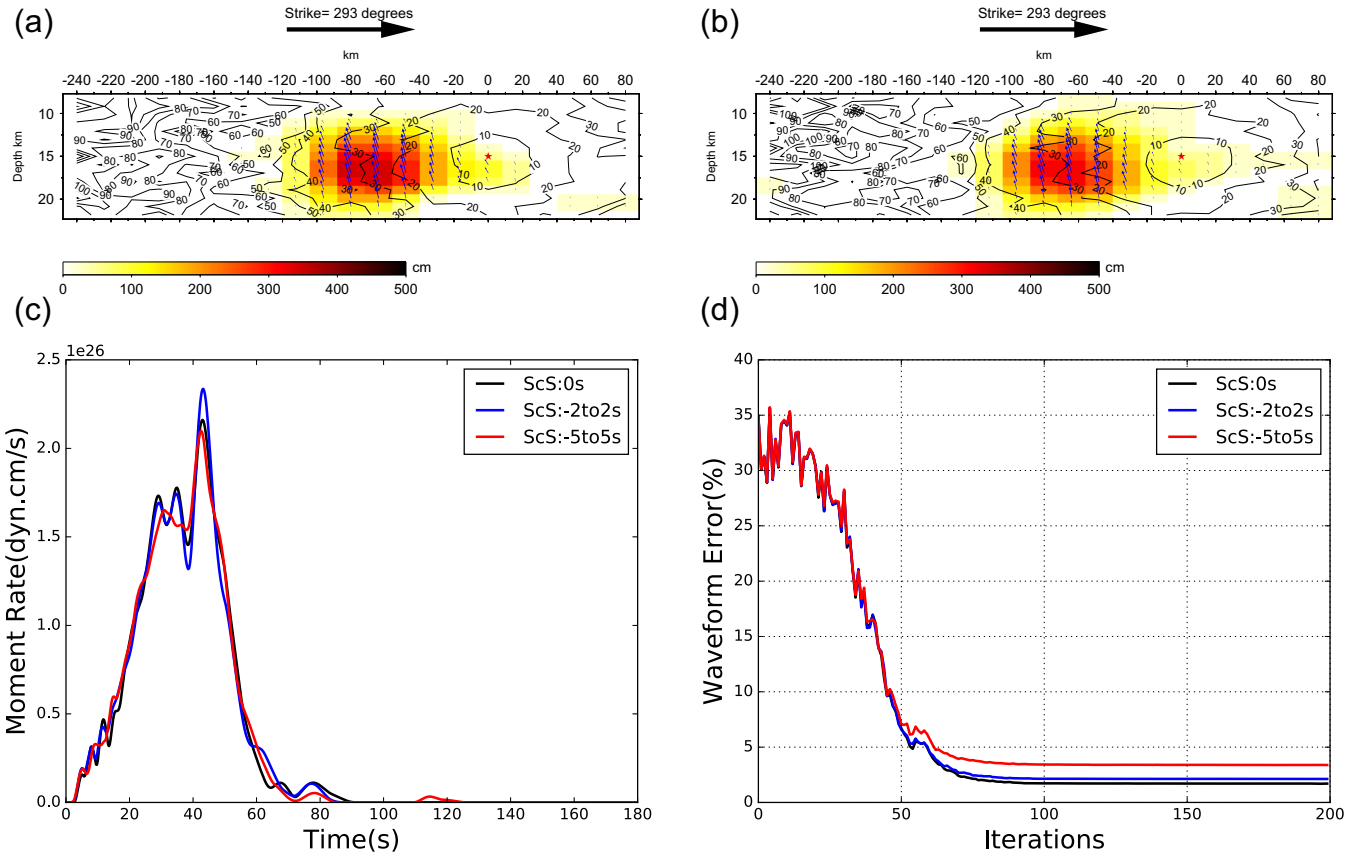


**Figure 10.** Influences of variations in  $ScS$  arrival times on finite fault inversions for the 2015 Nepal earthquake. Slip distribution and rupture front contours when  $ScS$  arrival time in the input data vary randomly (a) from  $-2$  to  $2$  s and (b) from  $-5$  to  $5$  s relative to Fig. 7(c), where  $ScS$  arrival time is  $0$ . The hypocentre is marked with a red star and the rupture time is indicated by black contours at intervals of  $10$  s. Blue arrows indicate inverted slip vectors. (c) Inverted moment rate function when  $ScS$  arrival time variation is  $0$  s (black),  $-2$  to  $2$  s (red) and  $-5$  to  $5$  s (blue). (d) Waveform misfits for these three inversion tests along iterations of simulated annealing inversion.

System (GPS) offsets, coral microatolls and seismic data have provided robust constraints on the slip distribution of this earthquake (Briggs *et al.* 2006; Konca *et al.* 2008). We will use the well-constrained slip distribution, which shows two main asperities of thrust motion on both sides of the epicentre, as a benchmark to test the impacts of core-reflected phases in our teleseismic waveform inversions.

We use  $39 P$  waves and  $43 SH$  waves for the inversion, all recorded at GSN stations with epicentre distances of  $50^\circ$ – $90^\circ$ . We conduct finite fault inversion with a  $160$  s time window using the Green's functions with and without core-reflected phases. We adopt the hypocentre from the US National Earthquake Information Center (US NEIC;  $97.01^\circ E$ ,  $2.07^\circ N$ ,  $30$  km), and extract a 1-D velocity model from Crust2.0 at the epicentre. Hsu *et al.* (2006) have explored the influence of the assumed fault geometry for this event, and found that the sensitivity of curved and planar fault geometries on the slip distribution is insignificant. Thus we assume a planar fault plane with a length of  $416$  km along strike ( $325^\circ$ ) and a width of  $300$  km along dip direction ( $10^\circ$ ), based on the GCMT result, discretized into  $260$  subfaults ( $26 \times 10$ ) of  $16$  km  $\times$   $30$  km. The rupture velocity ranges from  $1.5$  to  $2.5$  km  $s^{-1}$  at an interval of  $0.1$  km  $s^{-1}$ , the rise time varies from  $2$  to  $20$  s at an interval of  $1$  s, the slip changes from  $0$  to  $10$  m at an interval of  $0.2$  m and the rake angle is from  $0^\circ$  to  $180^\circ$  at an interval of  $2.5^\circ$  in the inversions.

In Fig. 11, we display the rupture models obtained from teleseismic inversions without and with core-phases (Figs 11c and d) along

with the models from previous studies (Figs 11a and b). Our results show that the inversion with the core-phases fits the waveforms better than that without these phases (Fig. 12). As an example, we look into greater details for  $SH$  waveforms recorded on four stations with different epicentral distances: FURI ( $58^\circ$ ), MALT ( $64^\circ$ ), OBN ( $71^\circ$ ) and KBS ( $86^\circ$ ). The modelled turning waves fit well at MALT (green background) and KBS (red background) stations (Figs 12a and b), which have  $ScS-S$  differential times of  $\sim 80$  s and  $\sim 10$  s, respectively. But for other stations, the synthetics (red traces) have time shifts with respect to the observations when  $ScS$  phases are not included, such as the recordings on FURI (blue background) and OBN (purple background) station in Fig. 12(a), which have  $ScS-S$  differential times of  $\sim 110$  s and  $\sim 50$  s, respectively. In short, the synthetics with the  $ScS$  phases have an overall better match with the data, both in arrival time and waveform shape.

When we compare our models (Figs 11c and d) to the model in Fig. 11(a) (Konca *et al.* 2008), derived from teleseismic  $P$  and  $SH$  waves, we can see that they are very different. Our models show two major asperities, one beneath Nias Island to the northwest and the other between Simeulue and Banyak Islands to the southeast, which are not observed in Fig. 11(a). This difference could be partially caused by different smoothing factors used in the teleseismic inversions, or by the different number of stations used ( $39 P + 43 SH$  in our study versus  $16 P + 10 SH$  in Konca *et al.* 2008). The locations of the two major asperities in our models are more consistent with the slip model of Briggs *et al.* (2006; Fig. 11b; derived

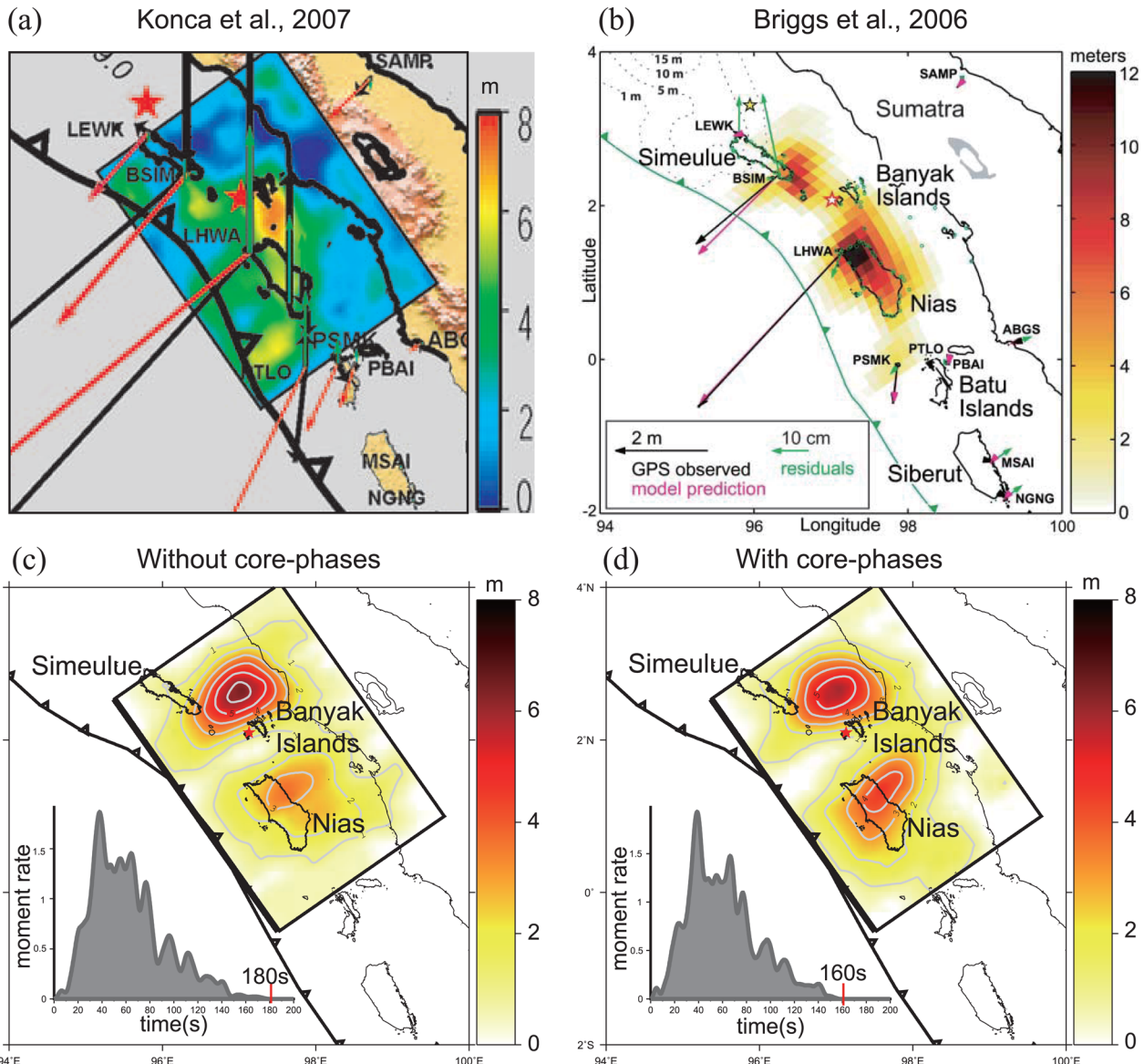


**Figure 11.** Comparison of finite fault inversions for the 2005 Nias–Simeulue earthquake. (a) Slip distribution from teleseismic data modified from fig. 5(a) in Konca *et al.* (2008). (b) Slip distribution from coral displacement and GPS data from fig. 5 in Briggs *et al.* (2006). (c,d) Slip distribution models and moment rate functions from this study using teleseismic  $P$  and  $SH$  data without core-reflected phases (c) and with them (d) in the Green's functions. Grey contours at 1 m slip intervals. Hypocentre location is shown with red star in all panels.

from coral displacement and GPS data) and the slip model of Konca *et al.* (2008; their fig. 5d; derived from teleseismic body wave, coral displacement and GPS data). In these models, the northwest asperity has a smaller peak slip amplitude than the southeast asperity, while our inversion derived without core-phases shows the opposite. However, when we include the core-phases the inversion clearly improves, and we obtain a cleaner slip distribution with comparable peak slips for both asperities. This improvement benefits from more accurate Green's functions with inclusion of  $PcP$  and  $ScS$ , which not only guarantee better waveform fits by accounting for interference effects between direct phases and core-reflected phases, but also provide a better coverage of the focal sphere by including core-reflected rays with different takeoff angles from direct rays in the source region. The theoretical differences between takeoff angles from  $P/S$  and  $PcP/ScS$  are displayed in Supporting Information Fig. S1(a), along with their traveltimes (Supporting Informa-

tion Fig. S1b). We should note that the peak slip amplitudes in our models are about half than those obtained geodetically, but this is a common occurrence when comparing seismic and geodetic finite fault inversions. The moment rate function obtained without core-phases Fig. 11(c) is slightly longer than that obtained with them Fig. 11(d). This is similar to the synthetic tests for the 2015 Nepal earthquake Fig. 8(a), suggesting that this is an artefact caused by no including core-reflected phases in the Green's functions. Thus, for the 2005 Nias–Simeulue earthquake, we prefer a source duration of 160 s Fig. 11(d) rather than 180 s Fig. 11(c).

Our results suggest that large-scale features are similar between the inversion with and without core-phases, but rupture models inverted with the core-phases are more consistent with results obtained from other independent studies. Even though there are trade-offs among rise time, slip magnitude and rupture velocity for the teleseismic inversions, the effects of the different Green's functions

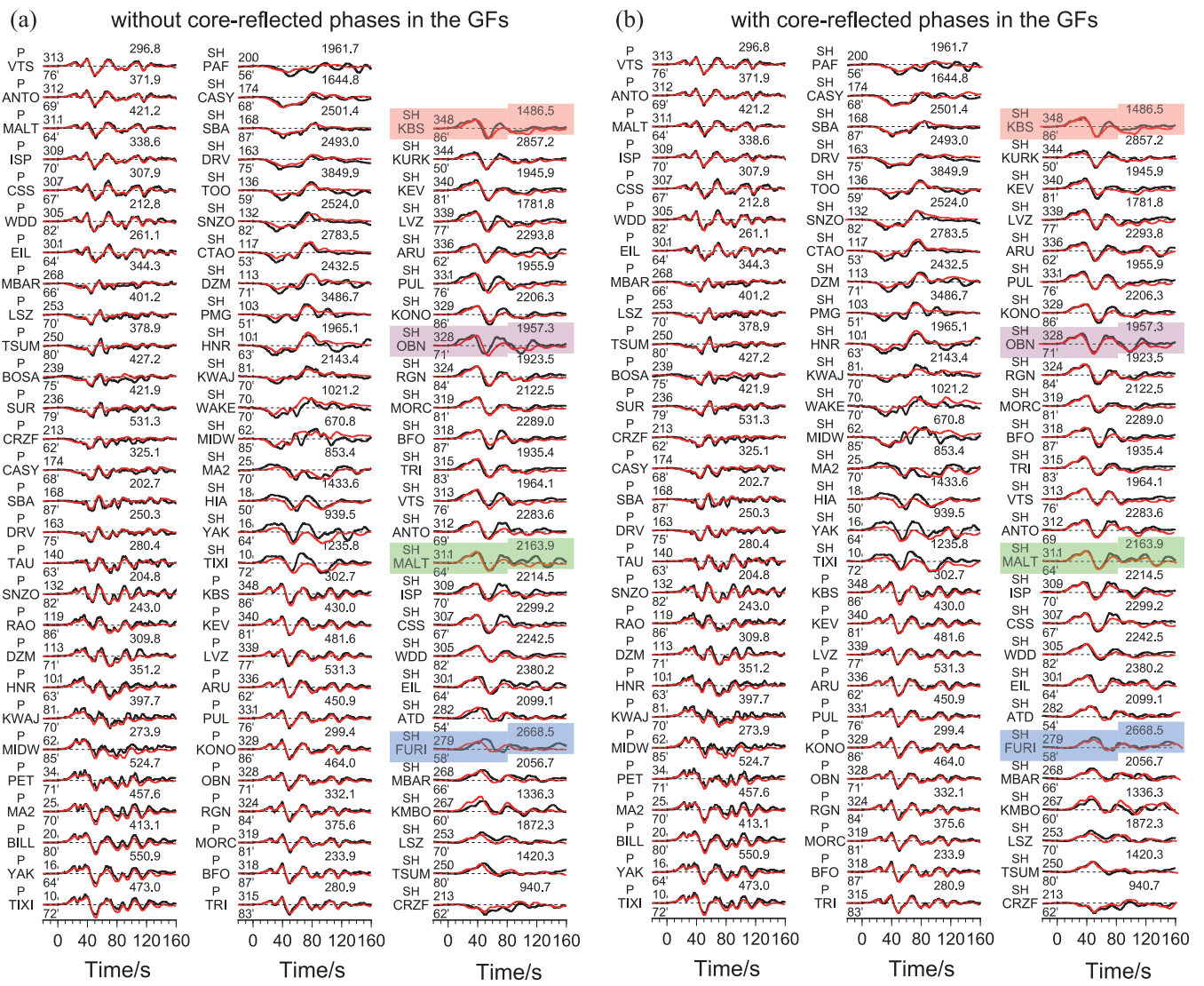


**Figure 12.** Waveform modelling for the 2005 Nias–Simeulue earthquake. Black traces are observations, red traces are synthetic displacement waveforms with no core-reflected phases in (a) and containing core-reflected waves in (b). The waveform type and station name are to the left of each trace. Numbers at the left of each seismogram are epicentral distance (under) and azimuth (upper) in degree and numbers at the right of waveforms are maximum amplitude in micrometer. Stations discussed in text for comparison purpose are highlighted with coloured backgrounds.

are large enough to be distinguished between the different rupture models.

## 6 DISCUSSION

We use a hybrid technique combining ray theory with a propagator matrix method, which allows to model each phase separately. In our approach, the differential times between direct and core-reflected phases could be easily added as free parameters in inversions, to further suppress the structure effects and improve our source study results in the future. Garcia *et al.* (2004) have successfully used a similar approach to model the complicated interferences between the different branches of PKP waves. This concept could be implemented for finite-source inversions using our new Green's functions. What's more, our technique allows us to calculate high frequency teleseismic body waves effectively, accounting for different crustal velocities around both of source region and receiver sites.

Our study suggests that core-reflected phases can be used in teleseismic inversions to provide better rupture process analyses.

Although the records for synthetic tests and application in the cases are derived from GSN stations, which have good coverage in the distribution of paths in distance and azimuth, the interference effects were still observed and the results were improved with inclusion of core-reflected phases. We would like to point out that the interference effects will be stronger if the distances and azimuths of records used in the inversions have a small range, as is typical for some seismic array techniques. For finite fault inversions, the arrival times of the core-phases become more consistent between different stations when the distance coverage is restricted in a narrow range thus even the core-reflected phases are easier attributed to the source effect. Special care should be taken in these cases, as it is easy to misidentify core-reflected phases as signals from rupture processes due to their similar slowness as direct phases.

## 7 CONCLUSIONS

We have developed a procedure for generating teleseismic Green's functions with both turning waves and core-reflected phases. A

comparison with full waveform synthetics (FK; Zhu & Rivera 2002) demonstrates that our approach is accurate and efficient. In the synthetic tests that mimic the 2008  $M_w$  7.9 Wenchuan earthquake, we have shown the improvements of considering core-reflected phases in Green's functions, especially for  $PcP$  phases. Another synthetic test on a rupture model of the 2015  $M_w$  7.8 Nepal earthquake demonstrates that the inclusion of core-reflected phases could produce a prolonged source time function, which is caused by not including core-phases in the Green's function.

When we applied our approach to the 2005  $M_w$  8.7 Nias–Simeulue earthquake, we found that neglecting core-reflected phases in the Green's functions not only produce worse waveform misfits, but also results in time shifts between the synthetic waveforms and the observations. These time shifts, attributed to the imperfect 1-D Green's functions (ignoring core-phases), will lead to artefacts in the slip model. Our preferred result with the new Green's functions, including turning and core-reflected phases, is more consistent with the slip models derived from joint inversion of surface deformation, GPS and teleseismic data (Briggs *et al.* 2006; Konca *et al.* 2008).

The inversion results for both synthetic and real data show that major features between rupture models derived with and without core-reflected phases are similar. However, when core-phases are included, the inverted waveform misfit is reduced and the slip models are more realistic. To obtain better Green's function for slip inversions, we have to calibrate the arrival time and amplitude of core-reflected phases, which can be affected by the 3-D earth structure. Such calibration can be obtained by using a moderate earthquake that is close to the main shock, for example, aftershocks or historical earthquakes.

## ACKNOWLEDGEMENTS

The teleseismic data used were obtained from Incorporated Research Institutions for Seismology (IRIS). This work made use of GMT software and Matplotlib (a Python 2-D plotting library) to generate figures. We thank Fares Mehoudi and Deepa Mele Veedu for their comments to improve our manuscript. This paper benefited from constructive review comments and helpful suggestions by Dr Sébastien Chevrot and another anonymous reviewer for which we are grateful. This study is supported by China 973 Basic Research Program 468 2014CB845901 and NSFC 41274069.

## REFERENCES

- Ammon, C.J., Lay, T., Kanamori, H. & Cleveland, M., 2011. A rupture model of the 2011 off the Pacific coast of Tohoku earthquake, *Earth Planets Space*, **63**, 693–696.
- Bassin, C., Laske, G. & Masters, G., 2000. The current limits of resolution for surface wave tomography in North America, *EOS, Trans. Am. geophys. Un.*, **81**, 897.
- Borgeaud, A.F., Konishi, K., Kawai, K. & Geller, R.J., 2016. Finite frequency effects on apparent S-wave splitting in the D'' layer: comparison between ray theory and full-wave synthetics, *Geophys. J. Int.*, **207**(1), 12–28.
- Bouchon, M., 1976. Teleseismic body wave radiation from a seismic source in a layered medium, *Geophys. J. Int.*, **47**, 515–530.
- Briggs, R.W. *et al.*, 2006. Deformation and slip along the Sunda megathrust in the great 2005 Nias–Simeulue earthquake, *Science*, **311**(5769), 1897–1901.
- Chen, Y. & Xu, L., 2000. A time-domain inversion technique for the temporal-spatial distribution of slip on a finite fault plane with applications to recent large earthquakes in the Tibetan Plateau, *Geophys. J. Int.*, **143**, 407–416.
- Chu, R., Zhu, L. & Helmberger, D.V., 2009. Determination of earthquake focal depths and source time functions in central Asia using teleseismic P waveforms, *Geophys. Res. Lett.*, **36**, L17317, doi:10.1029/2009GL039494.
- Cotton, F. & Campillo, M., 1995. Frequency domain inversion of strong motions: application to the 1992 Landers earthquake, *J. geophys. Res.*, **100**, 3961–3975.
- Dziewonski, A.M. & Anderson, D.L., 1981. Preliminary reference Earth model, *Phys. Earth planet. Inter.*, **25**(4), 297–356.
- Feng, G., Hetland, E.A., Ding, X., Li, Z. & Zhang, L., 2010. Coseismic fault slip of the 2008  $M_w$  7.9 Wenchuan earthquake estimated from InSAR and GPS measurements, *Geophys. Res. Lett.*, **37**, L01302, doi:10.1029/2009GL041213.
- Fielding, E.J., Sladen, A., Li, Z., Avouac, J.P., Burgmann, R. & Ryder, I., 2013. Kinematic fault slip evolution source models of the 2008 M7.9 Wenchuan earthquake in China from SAR interferometry, GPS and teleseismic analysis and implications for Longmen Shan tectonics, *Geophys. J. Int.*, **194**, 1138–1166.
- Garcia, R., Chevrot, S. & Weber, M., 2004. Nonlinear waveform and delay time analysis of triplicated core phases, *J. geophys. Res.*, **109**, B01306, doi:10.1029/2003JB002429.
- Hao, J., Ji, C., Wang, W. & Yao, Z., 2013. Rupture history of the 2013  $M_w$  6.6 Lushan earthquake constrained with local strong motion and teleseismic body and surface waves, *Geophys. Res. Lett.*, **40**, 5371–5376.
- Hartzell, S.H. & Heaton, T.H., 1983. Inversion of strong ground motion and teleseismic waveform data for the fault rupture history of the 1979 Imperial Valley, California, earthquake, *Bull. seism. Soc. Am.*, **73**, 1553–1583.
- Hartzell, S., Mendoza, C., Ramirez-Guzman, L., Zeng, Y. & Mooney, W., 2013. Rupture history of the 2008  $M_w$  7.9 Wenchuan, China, Earthquake: evaluation of separate and joint inversions of geodetic, teleseismic, and strong-motion data, *Bull. seism. Soc. Am.*, **103**, 353–370.
- Haskell, N.A., 1960. Crustal reflection of plane SH waves, *J. geophys. Res.*, **65**, 4147–4150.
- Haskell, N.A., 1962. Crustal reflection of plane P and SV waves, *J. geophys. Res.*, **67**, 4751–4768.
- Heidarzadeh, M., Murotani, S., Satake, K., Ishibe, T. & Gusman, A.R., 2016. Source model of the 16 September 2015 Illapel, Chile,  $M_w$  8.4 earthquake based on teleseismic and tsunami data, *Geophys. Res. Lett.*, **43**(2), 643–650.
- Helffrich, G.R., 1997. How good are routinely determined focal mechanisms? Empirical statistics based on a comparison of Harvard, USGS and ERI moment tensors, *Geophys. J. Int.*, **131**, 741–750.
- Hsu, Y.J. *et al.*, 2006. Frictional afterslip following the 2005 Nias–Simeulue earthquake, Sumatra, *Science*, **312**(5782), 1921–1926.
- Ji, C., Wald, D.J. & Helmberger, D.V., 2002. Source description of the 1999 Hector Mine, California, earthquake, Part I: Wavelet domain inversion theory and resolution analysis, *Bull. seism. Soc. Am.*, **92**, 1192–1207.
- Ji, C., Larson, K.M., Tan, Y., Hudnut, K.W. & Choi, K., 2004. Slip history of the 2003 San Simeon earthquake constrained by combining 1-Hz GPS, strong motion, and teleseismic data, *Geophys. Res. Lett.*, **31**, L17608, doi:10.1029/2004GL020448.
- Kikuchi, M. & Kanamori, H., 1986. Inversion of complex body waves-II, *Phys. Earth planet. Inter.*, **43**, 205–222.
- Kikuchi, M. & Kanamori, H., 1991. Inversion of complex body waves-III, *Bull. seism. Soc. Am.*, **81**, 2335–2350.
- Konca, A.O. *et al.*, 2008. Partial rupture of a locked patch of the Sumatra megathrust during the 2007 earthquake sequence, *Nature*, **456**(7222), 631–635.
- Langston, C.A. & Helmberger, D.V., 1975. A procedure for modelling shallow dislocation sources, *Geophys. J. Int.*, **42**, 117–130.
- Li, L., Lay, T., Cheung, K.F. & Ye, L., 2016. Joint modeling of teleseismic and tsunami wave observations to constrain the 16 September 2015 Illapel, Chile,  $M_w$  8.3 earthquake rupture process, *Geophys. Res. Lett.*, **43**(9), 4303–4312.
- Liu, C., Zheng, Y., Ge, C., Xiong, X. & Hsu, H., 2013. Rupture process of the Ms7.0 Lushan earthquake, 2013, *Sci. China Earth Sci.*, **56**, 1187–1192.
- McCaffrey, R., Zwick, P. & Abers, G., 1991. SYN4 program, *LASPEI Softw. Libr.*, **3**, 81–166.

- Nakamura, T., Tsuboi, S., Kaneda, Y. & Yamanaka, Y., 2010. Rupture process of the 2008 Wenchuan, China earthquake inferred from teleseismic waveform inversion and forward modeling of broadband seismic waves, *Tectonophysics*, **491**, 72–84.
- Ni, S. & Helmberger, D.V., 2003. Seismological constraints on the South African superplume; could be the oldest distinct structure on Earth, *Earth planet. Sci. Lett.*, **206**, 119–131.
- Olson, A.H. & Anderson, J.G., 1988. Implications of frequency-domain inversion of earthquake ground motions for resolving the space-time dependence of slip on an extended fault, *Geophys. J. Int.*, **94**, 443–455.
- Olson, A.H. & Apsel, R.J., 1982. Finite faults and inverse theory with applications to the 1979 Imperial Valley earthquake, *Bull. seism. Soc. Am.*, **72**, 1969–2001.
- Pratt, R.G., 1999. Seismic waveform inversion in the frequency domain, Part 1: Theory and verification in a physical scale model, *Geophysics*, **64**, 888–901.
- Ritsema, J., Ni, S., Helmberger, D.V. & Crotwell, H.P., 1998. Evidence for strong shear velocity reductions and velocity gradients in the lower mantle beneath Africa, *Geophys. Res. Lett.*, **25**, 4245–4248.
- Shao, G. & Ji, C., 2012. What the exercise of the SPICE source inversion validation BlindTest 1 did not tell you, *Geophys. J. Int.*, **189**, 569–590.
- Shen, Z.-K. et al., 2009. Slip maxima at fault junctions and rupturing of barriers during the 2008 Wenchuan earthquake, *Nat. Geosci.*, **2**, 718–724.
- Simons, M. et al., 2011. The 2011 magnitude 9.0 Tohoku-Oki earthquake: Mosaicking the megathrust from seconds to centuries, *Science*, **332**, 1421–1425.
- Sipkin, S.A. & Jordan, T.H., 1976. Lateral heterogeneity of the upper mantle determined from the travel times of multiple  $ScS$ , *J. geophys. Res.*, **81**, 6307–6320.
- Tsuboi, S., Komatitsch, D., Ji, C. & Tromp, J., 2003. Broadband modeling of the 2002 Denali fault earthquake on the Earth Simulator, *Phys. Earth planet. Inter.*, **139**, 305–313.
- Vallée, M., Charléty, J., Ferreira, A.M.G., Delouis, B. & Vergoz, J., 2011. SCARDEC: a new technique for the rapid determination of seismic moment magnitude, focal mechanism and source time functions for large earthquakes using body-wave deconvolution, *Geophys. J. Int.*, **184**, 338–358.
- Wald, D.J. & Graves, R.W., 2001. Resolution analysis of finite fault source inversion using one- and three-dimensional Green's functions: 2. Combining seismic and geodetic data, *J. geophys. Res.*, **106**, 8767–8788.
- Wei, S., Graves, R., Helmberger, D., Avouac, J.-P. & Jiang, J., 2012. Sources of shaking and flooding during the Tohoku-Oki earthquake: a mixture of rupture styles, *Earth planet. Sci. Lett.*, **333**, 91–100.
- Wookey, J., Kendall, J.M. & Rümpker, G., 2005. Lowermost mantle anisotropy beneath the north Pacific from differential  $S$ – $ScS$  splitting, *Geophys. J. Int.*, **161**, 829–838.
- Xu, X., Wen, X., Yu, G., Chen, G., Klinger, Y., Hubbard, J. & Shaw, J., 2009. Coseismic reverse- and oblique-slip surface faulting generated by the 2008  $M_w$  7.9 Wenchuan earthquake, China, *Geology*, **37**, 515–518.
- Yagi, Y., Nishimura, N. & Kasahara, A., 2012. Source process of the 12 May 2008 Wenchuan, China, earthquake determined by waveform inversion of teleseismic body waves with a data covariance matrix, *Earth Planets Space*, **64**, 13–16.
- Yu, Z., Ni, S., Wei, S., Zeng, X., Wu, W. & Li, Z., 2012. An iterative algorithm for separation of  $S$  and  $ScS$  waves of great earthquakes, *Geophys. J. Int.*, **191**, 591–600.
- Zhang, Y., Feng, W., Xu, L., Zhou, C. & Chen, Y., 2008. Spatio-temporal rupture process of the 2008 great Wenchuan earthquake, *Sci. China Ser. D: Earth Sci.*, **52**, 145–154.
- Zhu, L. & Rivera, L.A., 2002. A note on the dynamic and static displacements from a point source in multilayered media, *Geophys. J. Int.*, **148**, 619–627.

## SUPPORTING INFORMATION

Supplementary data are available at [GJI](#) online.

**Figure S1.** Theoretical takeoff angles (a) and arrival times (b) for direct and core-reflected phases vary with distance when the hypocentre depth is 30 km.

Please note: Oxford University Press is not responsible for the content or functionality of any supporting materials supplied by the authors. Any queries (other than missing material) should be directed to the corresponding author for the paper.